Highly Active and Stable OER Electrocatalysts Derived from Sr_2MIrO_6 for Proton Exchange Membrane Water Electrolyzers

María Retuerto[1,*], Laura Pascual[2], Jorge Torrero[3], Mohamed Abdel Salam[4], Álvaro Tolosana-Moranchel,[1] Diego Gianolio[5], Pilar Ferrer[5], Paula Kayser[6], Vincent Wilke[3], Svenja Stiber[3], Verónica Celorrio[5], Mohamed Mokthar[4], Daniel García Sanchez[3], Aldo Saul Gago[3], Kaspar Andreas Friedrich[3], Miguel Antonio Peña[1], José Antonio Alonso[6], Sergio Rojas[1,*]

[1]*Grupo de Energía y Química Sostenibles, Instituto de Catálisis y Petroleoquímica, CSIC. C/Marie Curie 2, 28049, Madrid, Spain*

[2]*Instituto de Catálisis y Petroleoquímica, CSIC. C/Marie Curie 2, 28049, Madrid, Spain*

[3]*Institute of Engineering Thermodynamics/Electrochemical Energy Technology, German Aerospace Center (DLR), Pfaffenwaldring 38-40, 70569 Stuttgart, Germany*

[4]*Chemistry Department, Faculty of Science, King Abdulaziz University, P. O Box 80200, Jeddah, 21589, Saudi Arabia.*

[5]*Diamond Light Source, Harwell Science and Innovation Campus, Didcot, OX11 0DE, UK*

[6]*Instituto de Ciencia de Materiales de Madrid, CSIC. C/Sor Juana Inés de la Cruz 3, 28049 Madrid, Spain.*

*e-mail: m.retuerto@csic.es, srojas@icp.csic.es

Proton exchange membrane water electrolysis is a promising technology to produce green hydrogen from renewables, as it can efficiently achieve high current densities. Lowering iridium amount in oxygen evolution reaction electrocatalysts is critical for achieving cost-effective production of green hydrogen. In this work, we develop catalysts from Ir double perovskites. Sr_2CaIrO_6 achieves 10 mAcm^{-2} at only 1.48 V. The surface of the perovskite reconstructs when immersed in an acidic electrolyte and during the first catalytic cycles, resulting in a stable surface conformed by short-range order edge-sharing IrO_6 octahedra arranged in an open structure responsible for the high performance. A proton exchange membrane water electrolysis cell is developed with Sr_2CaIrO_6 as anode and low Ir loading (0.4 mg_{Ir} cm^{-2}). The cell achieves 2.40 V at 6 A cm^{-2} (overload) and no loss in performance at a constant 2 A cm^{-2} (nominal load). Thus, reducing Ir use without compromising efficiency and lifetime.

Introduction

Green hydrogen, *i.e.*, the hydrogen produced through water electrolysis from renewable energy, has been identified as the key sustainable energy carrier for decarbonizing industry and transport sectors, including hard-to-abate subsectors. The demand for green hydrogen is therefore expected to increase drastically in the coming years from today's approximately 1% to 12% by 2050.[1] Proton exchange membrane water electrolysis (PEMWE) is regarded as the ideal technology to transform renewable energy into hydrogen.[2,3] PEMWE technology presents several advantages, including a fast response to fluctuations in renewable energies; operation at high current densities; production of high purity H_2 since the gas crossover rate is low; production of pressurized hydrogen during electrolysis reducing operational costs; and a compact design that is easy to stack and scale.

The electrolysis process is the splitting of H_2O, into H_2 and O_2 using electricity. In a PEMWE, H_2 is formed at the cathode ($4H^+ + 4e^- \rightarrow 2H_2$), and O_2 is produced at the anode ($2H_2O \rightarrow O_2 + 4H^+ + 4e^-$).[4] The latter reaction, *i.e.*, the oxygen evolution reaction (OER), is the limiting process, requiring large amounts of electrocatalyst to take place at reasonable overpotentials.[5] Due to the very strongly oxidizing environment in the anode of a PEMWE (low pH, high oxygen concentration, high potential and the presence of water), OER catalysts are based on Ru- or Ir-oxides. Although Ru catalysts display high initial activity, they are unstable during the OER.[6] Ir oxide-based catalysts display high OER activity and stability, with Ir-black, IrO_2, IrO_x-Ir, and $IrNiO_x$ being among the most active catalysts for the OER.[7,8] However, Ir is a scarce metal that is extracted as a minor byproduct of platinum, and its demand is growing (267,000 oz in 2021)[9]; therefore, it is extremely expensive ($6,300 per oz in 2021), with both its price and production subjected to strong fluctuations, posing a risk for the deployment and scaling up of PEM electrolyzers. Therefore, a great deal of interest has been placed on reducing the content of Ir in OER electrocatalysts.

Ir mixed oxides display comparable or higher OER Ir mass-specific activities than Ir simple oxides.[10–15] However, Ir mixed oxides lack structural stability during the OER, mainly due to the high solubility of the non-noble elements in aqueous-acid solutions. In recent years, many efforts have been devoted to understanding this effect and to identifying the species formed during the OER, since the performance of Ir-mixed oxides is not the same between them so the reconstructions have to be different. Most works in the literature report the formation of simple iridium phases such as Ir-O-OH, Ir-OH, IrO_x

and/or IrO_2 with different levels of amorphization, although the exact nature of such phases remains unknown.[12,16–20]

In this work, we synthesized Ir double perovskites, Sr_2CaIrO_6, Sr_2MgIrO_6, and Sr_2ZnIrO_6 with the Ir atoms in a high oxidation state ($Ir^{6+/5+}$). We monitored the stability of the catalysts during the OER using both *in situ* and *ex situ* approaches. We observed a reconstruction of the surface of the perovskites due to the rapid dissolution of alkaline cations, especially Ca, produced after immersion in the electrolyte and progresses during the first OER cycles under it stabilizes. Despite the removal of the alkaline cations, the skeleton of the original perovskite remains unaltered and the surface reconstructs into short-ordered corner and edge-sharing IrO_6 octahedra in a very open structure responsible for the high OER activity of Sr_2CaIrO_6, which is among the highest reported in the literature, especially when it is tested in a PEM electrolyzer.

Results and discussion

Crystal structure of the double perovskites. Sr_2MIrO_6 (M= Ca, Zn, Mg) displays an $A_2BB'O_6$ double perovskite structure with $P2_1/n$ monoclinic symmetry (the Rietveld refinement of the crystal structures is shown in Figure S1, Supporting Information (SI)). Sr_2MIrO_6 shows a regular arrangement of alternating corner-sharing MO_6 and IrO_6 octahedra with Sr cations occupying the voids between the octahedra (inset of Figure S1, SI). Sr_2CaIrO_6 presents 13(2)% disorder between the Ca and Ir along both B positions, while Sr_2ZnIrO_6 and Sr_2MgIrO_6 present slightly larger cationic disorder. In fact, the values of the interatomic distances in Sr_2CaIrO_6 (<Ir-O> = 1.937(5) Å and <Ca-O> = 2.248(5) Å) differ more between them than in the other two oxides (Table S2, SI), which explains the larger cationic ordering and indicates the stronger asymmetric character of the Ir-O-Ca bond and strong anion polarization. The values of the distances using XRD have to be taken carefully since oxygen does not have a strong x-ray scattering effect. However, these results are comparable to previous results reported by the group using neutron powder diffraction,[21,22] which is very reliable to differentiate between, for instance, Sr/Ca, Sr/Mg or oxygen positions and occupancy. The volume and cell parameters decrease in the order $Ca^{2+} > Zn^{2+} > Mg^{2+}$, which is in line with the evolution of the ionic radii of M^{2+} cations.

The surface composition and oxidation state of the Ir surface atoms of Sr_2MIrO_6 were analyzed by XPS. A thorough discussion of the assignment of the peaks of the Ir 4*f* core-level region can be found in section S4, SI. The binding energy (BE) of the Ir $4f_{7/2}$

core level in Sr_2CaIrO_6 is centered at approximately 64.4 eV, shifting to lower BE of approximately 62.7 eV for Sr_2MgIrO_6 and Sr_2ZnIrO_6. This is due to the different contributions of the Ir^{5+}/Ir^{6+} and Ir^{4+}/Ir^{3+} components (Figure S4, SI), with a higher contribution of Ir^{5+}/Ir^{6+} in Ca perovskite in comparation with Mg and Zn perovskites. These values are in line with the BE values reported for Ir perovskites with Ir^{5+} and Ir^{6+}, such as La_2LiIrO_6 and Ba_2PrIrO_6,[12,23] suggesting the presence of Ir^{6+} in Sr_2CaIrO_6 and Ir^{5+}/Ir^{6+} in Sr_2MgIrO_6 and Sr_2ZnIrO_6. This assignment is in line with the oxidation state obtained by XAS for these perovskites.[21,22]

The crystalline domain sizes of the double perovskites were calculated by XRD, obtaining a value of approximately 30 nm for all samples (Figure S1, SI). However, the TEM micrographs show the presence of larger particles (approximately 300 nm (Figure S2, SI)), indicating that such large particles are formed by the agglomeration of smaller crystallites (Table S3, SI).

Electrochemical performance. **OER activity and durability in RDE.** Figure 1a depicts the *i*R-corrected polarization curves for the catalysts normalized to the geometric area of the electrode. The OER activity follows the order Sr_2CaIrO_6 > Sr_2MgIrO_6 > Sr_2ZnIrO_6. A metric usually reported to benchmark the OER activity is the potential at a current density of 10 mA cm^{-2}.[24] Sr_2CaIrO_6 reaches 1.48 V to achieve this current density and Sr_2MgIrO_6 and Sr_2ZnIrO_6 1.49 V and 1.51 V, respectively. Note that the formation of bubbles over Sr_2CaIrO_6 is visible at 1.4 V (Inset Figure 1a). The potential to achieve 10 mA cm^{-2} with Sr_2CaIrO_6 is similar to the ones reported for the best performing Ir-mixed oxides in the literature, namely, $SrTi_{0.67}Ir_{0.33}O_3$, 6H-$SrIrO_3$ and $SrZrO_3$:$SrIrO_3$ (Zr:Ir 1:2),[13,14,25] see Figure 1d and Table S1 in the SI. Tafel slopes of approximately 33-38 mV dec^{-1} (Figure 1b) were obtained for Sr_2MIrO_6 (M=Ca, Mg, Zn). The low Tafel slopes indicate a fast kinetics of the catalysts, superior to most Ir mixed oxides (Figure 1d). In order to assess the specific catalytic activities, the currents have been normalized to the mass-specific surface areas (A_S), see Section S4.1. The results show that the specific activity of Sr_2CaIrO_6 is higher than that of Sr_2MgIrO_6 and Sr_2ZnIrO_6 (Figure S7, SI).

Concerning the Ir mass-specific activities, Sr_2CaIrO_6 reaches 900 A g^{-1}_{Ir} at 1.525 V, with Sr_2MgIrO_6 and Sr_2ZnIrO_6 reaching Ir mass-specific activity of 260 and 139 A g^{-1}_{Ir}, respectively (Figure 1c). Figure 1d and Table S1 compares these values with the literature, being Sr_2CaIrO_6 only surpassed by $SrZrO_3$:$SrIrO_3$ among Ir mixed oxides.[25] Finally, we obtained a turnover frequency (TOF) for Sr_2CaIrO_6 at 1.5 V of 0.71 s^{-1} (see

Section S6.5 in the SI for details concerning TOF calculation). This value compares well with values reported for IrO_2 particles.[8]

To evaluate the durability in RDE, Figure S8a in the SI depicts the initial OER activity of the three perovskites and their activity after 100 cycles. Since the activity remained stable, the most active catalyst, Sr_2CaIrO_6, was subjected to a longer stability test of 5000 OER cycles, recording a loss of 15% of its initial activity. Chronoamperometry tests were performed for 1 h at the potentials needed to reach a current density of 10 mA cm^{-2} (not *i*R corrected) and the activities remain stable during the tests (Figure S8b, SI).

The origin of the high OER activity of the Sr_2MIrO_6 catalysts has been previously ascribed to the presence of Ir atoms in the high oxidation state, namely, 6+ and 5+, which are reported to display high OER activity.[12,26] However, considering Ir oxidation state as the only descriptor of the OER activity should be taken cautiously since $Ir^{5+/6+}$ cations only stabilize in certain mixed oxides that are unstable during OER under acidic conditions and result in the formation of $Ir^{3+/4+}$ phases. Recent reports suggest that the long-term OER activity of iridium mixed oxides accounts for the simple iridium oxide phases formed during the OER,[16–20] especially short-range order phases, thus questioning the relevance of the oxidation state of Ir in the mixed oxide.[27] However, this view fails to explain why the OER activities of iridium mixed oxides depend on their initial composition and structure. In this work, for instance, Sr_2CaIrO_6 records higher activity than Zn and Mg catalysts. In view of this, we carefully monitored the evolution of Sr_2CaIrO_6 (the most active catalyst reported in this work) during different stages of the reaction with the aim of unveiling the evolution and nature of the iridium oxide phases formed during the OER.

Evolution of Sr_2CaIrO_6 after immersion in 0.1 M $HClO_4$ electrolyte. A reconstruction of the catalyst surface commences after immersion of the perovskite in the acidic electrolyte. Figure 2 shows the selected identical location-TEM (IL-TEM panel) images of Sr_2CaIrO_6 obtained before (Figure 2a, IL-TEM panel) and after 5 min of immersion in 0.1 M $HClO_4$ (Figure 2b, IL-TEM panel), named Sr_2CaIrO_6-Elec. Before discussing the results, it is important to note that TEM analysis of the very large particles was not possible due to the intrinsic limitations of the technique. The shape of the particles remains stable, but a slight decrease in the size of the particles (approximately 5%) can be observed. The elemental EDX mappings of Sr_2CaIrO_6 and Sr_2CaIrO_6-Elec are shown

in Figure 2a and b (EDX panel). As expected, fresh Sr_2CaIrO_6 displays a homogeneous and stoichiometric distribution of Sr, Ca, Ir and O across the particles. On the other hand, the EDX mappings of Sr_2CaIrO_6-Elec (Figure 2b and Figure S10, SI) reveal a heterogeneous distribution of the elements, showing regions with Sr, Ca, Ir and O (with a partial loss of Ca and Sr), along with regions where only Ir and O can be found. The SAED analysis of the regions containing Sr, Ca, Ir and O shows several diffraction rings, corresponding to Sr_2CaIrO_6 and IrO_2 (Figure 2b left, SAED panel). On the other hand, the SAED of the particles containing only Ir and O shows two broad rings (2.7 and 1.5 Å) ascribed to amorphous IrOOH (Figure 2b right, SAED panel).[29,30]

The dissolution of Sr and Ca was confirmed by analysis of the composition of the electrolyte by ICP-OES (Table S4, SI). After 10 min of immersion in 0.1 M $HClO_4$ approximately 50% of Ca, along with a small fraction of Sr, dissolves in the electrolyte. The surface composition of Sr_2CaIrO_6-Elec was analyzed by XPS (Figure 2b, XPS panel and Figure S11, SI). The relative surface concentration of Ca and Sr decreases, confirming their dissolution. The Ir 4*f* core-level spectrum of Sr_2CaIrO_6-Elec shifts to a lower binding energy than that of the fresh sample (Figure S12, SI). The deconvolution of the spectrum reveals that the shifting accounts for the increasing intensity of the peaks ascribed to Ir^{3+} and Ir^{4+} species, most likely IrOOH and IrO_2, which become the main Ir species on the surface of Sr_2CaIrO_6-Elec. Nonetheless, Ir^{5+}/Ir^{6+} species are still observed, indicating that either the extension of the surface reconstruction is limited to a few layers (note that the XPS signal carries information from several layers of the catalyst, a depth of approximately 2-3 nm) and/or particles of the original perovskite that resist to the electrolyte. The analysis of the O 1*s* core-level spectra is shown in Figure S13, SI. Similar results were obtained for Sr_2ZnIrO_6 (see Table S4, Figures S11-S13, SI); however, the extend of the dissolution of Zn catalyst is less significant than that observed for the Ca catalyst.

The presence of the perovskite phase in Sr_2CaIrO_6-Elec was further confirmed by XRD (Figure S14, SI). The absence of diffraction lines for the Ir^{4+}/Ir^{3+} phases reveals that the IrOOH and IrO_2 phases in the surface are very amorphous, lacking long-range order. The evolution of the structure during immersion in the electrolyte was further monitored with *in situ* XAS. Figure S15 in the SI shows the Ir L_3-edge spectra for Sr_2CaIrO_6 and Sr_2CaIrO_6-Elec. The small change in the intensity of the edge indicates that immersion in the electrolyte leads to a change in Ir coordination. The low intensity of the change indicates that only a small fraction of the material is subjected to this change. There is no

clear shift in the peak, so the overall oxidation state of the Ir atoms in Sr_2CaIrO_6 remain stable.

In summary, the reconstruction of Sr_2CaIrO_6 commences during immersion in the electrolyte. The dissolution of the Ca and Sr cations leads to the formation of several surface layers of amorphous Ir-O_x-H_y phases in which Ir is more reduced than in the original perovskite. The extent of this transformation is limited to the surface, with most of the perovskite particles remaining unaltered during immersion.

Evolution of Sr_2CaIrO_6 after 100 OER cycles. The stability of Sr_2CaIrO_6 was studied by analyzing the composition and structure of the catalyst recovered after 100 OER cycles (Sr_2CaIrO_6-100) at 10 mV s^{-1} between 1.2 and 1.7 V *vs*. RHE. The XPS analysis of Sr_2CaIrO_6-100 reveals that the loss of Ca and Sr cations from the catalyst surface is more severe, with most of the Ir atoms in Ir^{3+}/Ir^{4+} oxidation states, although $Ir^{5+/6+}$ species are also observed (Figure 2c, XPS panel and Figures S11 and S12, SI). Note that the XRD of Sr_2CaIrO_6-100 reveals that the bulk crystalline structure is still the perovskite (Figure S14d, SI) and that diffraction lines for IrO_2 or IrOOH are not observed. However, it can be noticed a slight decrease of the crystalline domain size of the perovskites with cycling (Table S6).

Figure 2c (IL-TEM panel) shows that the general shape of the particles after 100 cycles remains unaltered. However, a closer inspection of the images reveals that the particles evolved to a hollow-open structure, indicating that the dissolution of Ca and Sr does not result in the collapse of the perovskite structure, forming a dense material; instead, the skeleton of the perovskite remains stable (Figure 3). EDX analysis of these hollow regions (Figure 3f) reveals that they only contain Ir and O, and their SAED shows the broad diffraction rings ascribed to IrOOH (Inset Figure 3d). In fact, the formation of these open structures is in line with the larger mass-specific surface areas obtained from the ECSA after immersion of the catalysts in the electrolyte compared to the fresh catalysts (see further discussion in Table S3 and Section S4.2).

Note that the formation of this kind of open structures is less evident for Mg and Zn perovskites (Figure S18, SI), possibly because the dissolution of Mg and Zn cations is slower than Ca. Also, this kind of reconstruction was not observed for similar Ir-mixed oxides. For instance, $SrCo_{0.9}Ir_{0.1}O_{3-\delta}$, Sr_2IrO_4 and $R_2Ir_2O_7$ reconstruct in corner-shared and under-coordinated IrO_6 octahedrons, responsible for their high activities;[16,17,19] $SrIr_{0.8}Zn_{0.2}O_3$ perovskite experiences an OER-induced metal to insulator transition that

reduces its OER activity after 800 cycles;[20] in other oxides, such as Sr_2CoIrO_6, there is a deposition of an IrO_x layer on the surface;[26,31] La_2LiIrO_6 evolves into IrO_2 particles at the surface;[12] and 9R-$BaIrO_3$ shows the initial formation of IrO_x nanoparticles, which evolve into amorphous $Ir^{4+}O_xH_y/IrO_6$ octahedrons and then to amorphous $Ir^{5+}O_x/IrO_6$ octahedrons on the surface.[18] This observation suggests that the nature of the cation at the B sites, rather than Sr at the A sites, contributes to the stability and nature of the phases formed during the reconstruction. The larger size, different nature, and the asymmetric character of the Ir-O-Ca bonds, make Ca^{2+} cations less likely to be accommodated at the B sites; being prone to be removed faster than the other cations during the process. The rapid dissolution of Ca leads to voids that are not occupied by vicinal Ir cations, probably because they are rapidly filled by hydroxonium (H_3O^+) ions,[16,32–34] thereby stabilizing the hollow structure of nanosized (short-range order) clusters of IrO_6 octahedra.

The local morphology of the hollow regions was further studied by aberration-corrected STEM-HAADF. These regions display a short-range order of a few angstroms, as shown in the Fourier fast transform (FFT) and in the filtered image (Figures 3g and 3h). These small domains are formed by groups of Ir cations with interplanar distances of 2.7 Å similar to those of d(101) of IrOOH, in which IrO_6 octahedra share edges (see inset of Figure 3h). Previous reports have discussed the correlation between the OER activity and the structure (connection) between the IrO_6 octahedra, with edge-sharing[30,34–37] and face-sharing[13,35] octahedra displaying the highest OER activity. The aberration-corrected analyses, and the *in situ* XAS experiments (see below) show that edge-sharing IrO_6 octahedra are the main phase in the hollow regions of the reconstructed catalyst. As discussed elsewhere, see references above, edge-sharing IrO_6 octahedra with shorter Ir-Ir distances display high OER performance.

Evolution of Sr_2CaIrO_6 after 2000-5000 OER cycles. The evolution of Sr_2CaIrO_6 during 2000 OER cycles (Sr_2CaIrO_6-2000) was monitored by *in situ* XAS. The Ir L_3-edge XANES signal of Sr_2CaIrO_6-Elec and Sr_2CaIrO_6-2000 are shown in Figure 4a together with IrO_2 standard. Figure 4b shows a shift of the white line position towards lower energies and an increment of the white line intensity at 11220 eV on spectra measured during the 2000 cycles, showing the correlation of this trend with a gradual change of Ir oxidation state and coordination geometry during the OER, excluding a quick phase transition. The energy shift from 11222.0 eV to 11220.1 eV indicates a partial reduction of Ir from 6+ to 4+, consistent with the gradual formation of IrOOH and/or IrO_2

species on the surface of Sr_2CaIrO_6. In fact, IrO_2 white line position has been measured at 11219.6 eV.

The evolution of the Fourier transform (FT) from the Ir L_3-edge extended X-ray absorption fine structure (EXAFS) signals during cycling is depicted in Figure 4c. First, the intensity of the first coordination shell progressively decreases with increased cycling. This is consistent with the higher intensity of the first coordination shell of Sr_2CaIrO_6 than that of IrOOH. However, more evident differences are observed in the second coordination shell region, between 2.5 and 3 Å. To evaluate the changes in this region, the EXAFS spectra of Sr_2CaIrO_6, IrO_2 and IrOOH have been simulated from reference data and compared with Sr_2CaIrO_6-Elec and Sr_2CaIrO_6-2000 (Figure 4d). The spectrum of Sr_2CaIrO_6-Elec was fitted starting from a crystallographic structure of the perovskite. The fit resulted in an excellent match between experimental and simulated data as it can be appreciated in Figure S16 and Table S7. Due to the complexity of the material, the presence of mixed phases, and the interference of contributions from a high number of scattering paths, a proper fit on the spectrum of Sr_2CaIrO_6-2000 could not be performed. Nevertheless, it is worth noticing that the signals of Sr_2CaIrO_6-2000 show an evolution across the whole radial distance range, but more evident in the second coordination shell region, where contributions from Ir-Ir paths for IrO_2 and IrOOH (see Figure 4d and Figure S17).[8,27,38] This observation is compatible with the formation of IrO_2 and IrOOH phases, confirming the results obtained by TEM and XPS.

Finally, Sr_2CaIrO_6 recovered after 5000 OER cycles (Sr_2CaIrO_6-5000) was analyzed. As shown in Figure 2d (IL-TEM panel) the particles appear more agglomerated. The observation of the open structures is more frequent than after 100 cycles (Figure S19, SI). The SAED pattern of the hollow regions displays halos at 2.7 and 1.5 Å (Figure 2d (SAED panel)) more diffuse than those obtained for Sr_2CaIrO_6-100 and Sr_2CaIrO_6-Elec, which suggests the continuous loss of local ordering. The agglomeration of the particles and/or the loss of local ordering can explain the 15% loss in activity observed after 5000 cycles (Figure S8a, SI). The XPS and ICP-analysis of the electrolyte of Sr_2CaIrO_6-5000 are similar to that of Sr_2CaIrO_6-100, indicating that after 100 cycles the changes during OER are into a more amorphous morphology, but there is no more cations dissolution.

Performance and stability of a Sr_2CaIrO_6 anode during PEMWE. Since Sr_2CaIrO_6 recorded the highest OER activity in RDE among the studied oxides, it was chosen to be tested in the electrolysis cell. Catalyst-coated membranes (CCMs)

308 employing Sr_2CaIrO_6 as the anode catalyst (1 $mg_{cat}cm^{-2}$ or 0.4 mg_{Ir} cm^{-2}) were produced
309 by spray coating, and then they were tested in a 4 cm^2 active area PEMWE single cell. A
310 polarization curve recorded up to 6 A cm^{-2} at 80 °C and ambient pressure is shown in
311 Figure 5a. The curve reveals a peak performance of 6 A cm^{-2} at 2.40 V and shows a linear
312 slope, indicating the absence of significant mass-transport limitations or rapid
313 degradation processes. This demonstrates that the high OER performance obtained in the
314 RDE configuration is also attained in the electrolytic cell. With a cell potential of 1.81 V
315 at the nominal current density of 2 A cm^{-2}, the performance is comparable to the most
316 recent reports of PEMWE[39–42] with an Ir loading comparable or even lower than those
317 used in commercial CCMs.[43] As shown in Figure 5a, the performance of our cell is
318 analogous to the best PEMWEs with the same MEA, i.e., Nafion 212, and operating
319 conditions; 80 °C and ambient pressure.[42,44–46] Most of these studies were conducted
320 using a higher Ir loading (1-2 mg_{Ir} cm^{-2}) than our PEMWE (0.4 mg_{Ir} cm^{-2}). Only recent
321 works by Hegge et al.[46] and Bernt et al.[47] and Möckl et al.[48] reported PEMWE with lower
322 Ir loadings, also resulting in high performant CCMs. Given that none of the reports in the
323 literature use 0.4 mg_{Ir} cm^{-2}, an in-house reference CCM with commercial Ir_{black} (0.4 mg_{Ir}
324 cm^{-2}) has been produced using the coating media recipe reported by M. Bernt et al.[42] The
325 polarization curves, high frequency resistances (HFR) and Tafel plots obtained are
326 presented in Figure S20. As deduced from the results presented in S13, the high cell
327 performance can be mostly attributed to the enhanced electrochemical properties of the
328 Sr_2CaIrO_6 electrode.
329 Last, to evaluate catalyst stability, a Sr_2CaIrO_6 anode cell was tested at a constant
330 nominal load of 2 A cm^{-2}. The recorded cell potential and cell temperature are shown in
331 Figure 5b. The cell shows an activation period during the first 50 h, but afterward, E_{cell}
332 remains practically constant for 450 h, confirming that the electrocatalytic active phase
333 derived from Sr_2CaIrO_6 is stable under PEMWE conditions, which was also shown in the
334 RDE measurements.
335
336 In this work, we show that Sr_2MIrO_6 (Ca, Mg, Zn) perovskites, especially
337 Sr_2CaIrO_6, generate OER electrocatalysts which are among the most active ones reported
338 in the literature, as shown by the RDE and PEMWE test results. In order to understand
339 the origin of such high activity, the evolution of Sr_2CaIrO_6 during the OER was
340 thoroughly studied by *ex situ* and *in situ* techniques. During immersion in the electrolyte,

and during the first OER cycles, the surface of the perovskite suffers severe reconstruction that is triggered by the dissolution of Ca and Sr cations into the electrolyte. This dissolution results in the formation of an outer layer of Ir-rich phases with Ir atoms in the $3^+/4^+$ oxidation state. The fast removal of alkaline cations from the structure of the perovskite results in voids that are filled by H_3O^+ molecules, thus stabilizing the formation of the short-range ordered regions of edge-sharing IrO_6 octahedra. The formation of such regions conforms an open structure at the surface of the perovskite which is the responsible for the very high OER activity and durability of the catalyst. The high OER activity and durability of the catalyst obtained from Sr_2CaIrO_6 allows for a significant reduction of the use of Ir down to 0.4 mg_{Ir} cm^{-2} at the anode of PEMWE. As a result, the bottleneck that represents the use of a scare material such as Ir for the scaling up and manufacturing PEMWEs can be avoided, making this technology the most suitable for the production of green hydrogen.

Methods

Synthesis of double perovskites

Sr_2CaIrO_6, Sr_2MgIrO_6 and Sr_2ZnIrO_6 were synthesized by sol-gel method following references.[21,22] $Sr(NO_3)_2$, $CaCO_3$, MgO, ZnO and IrO_2 were dissolved in a solution of citric acid and HNO_3 under strong magnetic stirring (note that IrO_2 remained dispersed). The suspension was slowly evaporated at 100 ºC leading to an organic resin in which the cations are homogeneously distributed. After complete evaporation of the solvents, the resulting resins were dried at 140 ºC under static air and then heated at 600 ºC under static air for 12 h in order to decompose the organic materials and eliminate the nitrates, obtaining reactive precursors. Then the precursors were then treated at 800 ºC/ 12 in O_2 flux. Subsequently, the precursors were heated under high oxygen pressure (200 bar) at 900 ºC/ 12 h to obtain Ir^{6+} perovskite oxides.

Physicochemical characterization

Phase identification and crystallite size were determined by x-ray powder diffraction (XRD). XRD patterns were collected on a X'PertProPAN analytical diffractometer using CuK_α radiation (λ = 1.5418 Å, 45 kV, 40 mA). The refinement of the crystal structures was performed using the Rietveld method and the Fullprof crystallographic program.[50,51]

Transmission electron microscopy (TEM), high-resolution electron microscopy (HRTEM), scanning transmission electron microscopy (STEM) and x-ray energy dispersive spectra (EDS) were recorded in a JEOL 2100 field emission gun transmission electron microscope operating at 200 kV and equipped with an EDX spectrometer Oxford INCA Energy 2000 system. The specimen was prepared by depositing aliquots of the desired sample onto a Cu grid supporting a lacey carbon film. Identical-Locations TEM (IL-TEM) was used to analyze the evolution of the catalysts at different stages during the OER.[52] To acquire the SAED patterns, low-dose illuminations conditions were used to avoid sample decomposition or other known effects such as the reduction of IrO_x to metallic Ir.

X-ray photoelectron spectra (XPS) were recorded with a VG Escalab200R electron spectrometer equipped with a Mg-Kα (hυ=1253.6 eV) X-ray source. Powdered samples of the electrocatalysts were dispersed in a Nafion-free ink and deposited on a carbon double-sided adhesive tape supported on a stainless-steel holder. The same holder-supported catalyst was used in different electrochemical treatments: fresh catalyst, immersed in the electrolyte during 10 minutes, performing 5, 100 and 5000 cycles of OER between 1.2 and 1.7 V vs. RHE at 50 mVs^{-1}. After every treatment, the sample was washed with water, dried at room temperature, and outgassed under a residual pressure of 10^{-6} mbar for 1 h in the XPS pre-chamber. Then, the samples were transferred into the analysis chamber and analysis begun when the residual pressure reached 10^{-8} mbar. The C1*s* peak due to the carbon double-sided adhesive tape and carbon black from the ink was set at 284.6 eV and used as reference. Peak intensities were estimated by calculating the integral of each peak after subtraction of a Shirley-shaped background and fitting the experimental peaks to a combination of Lorentzian and Gaussian curves. This fitting was based on bibliographic results of perovskite and related compounds; three different components were considered for the Ir $4f_{7/2}$ core level: Ir^0/Ir^{3+}, restricted to the range 61.2-62.2 eV, Ir^{4+}, restricted to the range 62.2-63.2 eV, and Ir^{5+}/Ir^{6+}, restricted to the rage 63.2.0-64.4 eV (see S7, SI). Besides, a ratio of 3:4 was imposed for the area of the $4f_{5/2}$:$4f_{7/2}$ spin-orbit doublets, which should be of the same FWHM for the same Ir species, and the constrained ranges

for the $4f_{5/2}$ components were shifted by 3 eV. Finally, the FWHM was maintained under 2.5 eV for all the components. Surface composition was determined using the integrated peak areas and the corresponding Wagner sensitivity factors.[53]

X ray Absorption Spectroscopy (XAS) measurements were performed at room temperature at Diamond Light Source (UK) on the B18 beamline.[54] Data were collected at Ir L_3-edge (E = 11215 eV) using a double crystal Si111 monochromator and Cr-coated mirrors. The measurements were performed in transmission mode using as detector 3 ion chambers with a gas mixture of Ar and He (80mbar, 240mbar, 240mbar of Ar resulting in absorption of ca 15%, 50%, 50% respectively). For *in situ* XAS measurement, the samples were loaded into a custom-made electrochemical cell, available on B18 beamline and with a design based on the cell developed by Sardar et al.[55] Electrochemical measurement were collected with an IVIUM potentiostat, using Au wire as counter electrode and Ag/AgCl as reference electrode. XAS data were collected in the energy range from 11015 to 11914 eV with a continuous QEXAFS acquisition mode and a constant energy step of 0.3 eV. The duration of a single scan was ca. 3 minutes. The scans were collected continuously while subjecting the sample to continuous cyclic voltammetry scans between 1.2 and 1.7 V_{RHE}. XAS data treatment (including normalization, extraction of χ(k) and Fourier Transform) was performed with Athena software from Demeter package.[56] For the analysis of trends on the whole series of data a custom python script was used to monitor position and intensity of the normalized spectra whiteline. EXAFS signals for three reference structures were simulated by calculating the main scattering paths and their contributions with FEFF6 code.[57] The sum of most relevant paths was then calculated within Artemis software, using ΔE_0 and Δr fixed to zero, S_0^2 fixed to 1 and Debye-Waller factors starting from 0.003 and increasing as a function of the path length R_{eff}.

Electrochemical characterization

An Autolab PGstat 302N potentiostat/galvanostat was used to test the electrochemical performance of the oxides. The measurements were performed using a standard three-compartment glass cell and a rotating disk electrode (RDE) (Pine Research Instruments). A graphite bar was used as the counter electrode. An Ag/AgCl (3 M) electrode was used as the reference electrode. The oxides were deposited as an ink on a glassy carbon working electrode. The ink was prepared by mixing the oxides with carbon black (Vulcan-XC-72R) to improve the electrical conductivity. The mixture was dispersed in tetrahydrofuran (THF) and 5% Nafion and sonicated with an Ultrasonic Processor UP50H (Hielscher). The composition of the ink was 5 mg_{oxide}, 1 mg_{vulcan}, 0.03 mL_{Nafion} and 0.97 mL_{THF}. 10 µL of ink were dropped onto the electrode of 0.196 cm^2 of area, with a catalyst loading of 0.25 $mg_{oxide}\,cm^{-2}$. Since pure perovskite phases were obtained, the Ir content in Sr_2CaIrO_6, Sr_2MgIrO_6 and Sr_2ZnIrO_6 is 38.2 wt.%, 39.4 wt.% and 36.3 wt.%, respectively. Therefore, the Ir loadings are 0.096, 0.099 and 0,090 $mg_{Ir}\,cm^{-2}$ for Sr_2CaIrO_6, Sr_2MgIrO_6 and Sr_2ZnIrO_6, respectively.

The OER was initially assessed by recording cyclic voltammograms between 1.1 and 1.7 V_{RHE} at 10 mVs^{-1} and a rotation rate of 1600 rpm. The measurements were performed in an O_2 saturated 0.1 M $HClO_4$ electrolyte to assure the O_2/H_2O equilibrium at 1.23 V. The OER kinetic curves were capacitance-corrected by using the average of the anodic and cathodic curves and *i*R-corrected by using the formula $E\text{-}iR_{corrected} = E_{applied} - iR$. In this formula i is the current and R is the ohmic electrolyte resistance (R ~29 Ω) as obtained

from Electrical Impedance Spectroscopy (EIS) at open circuit voltage. RDE durability tests were performed by recording 5000 consecutive cycles between 1.2 and 1.7 V_{RHE} at 10 mVs^{-1}, or by recording a chronoamperometric program fixing the current density at 10 mA cm^{-2} and monitoring the evolution of the potential during 1 hour. For the preparation of the cycled catalysts that are used for *post-mortem* characterization (XRD, XPS, etc) a large quantity of the catalysts mixed with vulcan were deposited on top of a carbon planchet. Then the catalysts were scraped off the planchet.

CCM preparation and PEMWE measurements

The catalysts coated membranes (CCMs) were prepared by the wet spraying technique using a vacuum heating table (Fuel Cell Store) to hold the Nafion 212 PEM substrate in place and heat it to 100°C during deposition. The distance between spraying nozzle and substrate was kept at. 6 cm, and the ink deposition rate was limited to 2 – 3 min mL^{-1}. The inks were prepared by mixing 1 mg of catalyst in 1 mL of ultra-pure H_2O (MiliQ, 18 MΩ/cm) and the desired amount of Nafion® D521 solution (5 wt.% in lower aliphatic alcohols and water) to achieve an ionomer content of 25 and 30 wt.% in the dry anode and cathode layer, respectively. The mixture was sonicated for at least 1 hour until the catalyst was well dispersed. 1 mL of isopropanol (IPA, ACS reagent, ≥99.5%) was added and the mixture was sonicated for 10 minutes to reach the adequate dispersion and homogeneity of the ink. This process was scaled up to the desired volume of ink. Subsequent to spraying and drying, the CCM was hot pressed at 5 MPa and 125 °C. The resulting loading of Ir at the anode was 0.4 mg cm^{-2} and the loading of Pt at the cathode was 0.4 mg cm^{-2}.

Ca and Sr will leach out in the process of OER electrolysis and could affect strongly the PEMWE performance, likely due to Sr and Ca cations displacing protons in the ionomer and PEM. Therefore, as it is always the case when testing any pristine CCM for PEMWE with a newly developed OER catalyst, the CCM goes through a protocol of activation, which involves an extensive chemical cleaning in diluted H_2SO_4 and electrochemical cycling, until the performance of the PEMWE does not change anymore. At this point the Sr and Ca on the surface of catalyst have been completely leached out posing no danger in affecting the PEMWE performance, as we later demonstrate in the durability test.

The CCMs were tested in two different PEMWE setups. The first one is optimized for screening cell components, recording polarization curves, and measuring electrochemical impedance spectroscopy (EIS). Water is fed passively, via natural convection. This ensures stable, steady conditions which are especially important for EIS. The second PEMWE setup is optimized for long term measurements and the anode and cathode water flow rate was 2.5 L/h. On both the anode and cathode side, a Ti porous sintered layer (PSL) on Ti mesh (PSL/mesh-PTL) compound PTL produced by diffusion bonding[58] coated with Pt[59] was deployed. On the cathode, a carbon paper sheet (Spectracarb 2050A-1050) was used as an additional layer contacting the cathode catalyst layer on one, and the PTL on the other side. On both the anode and cathode side Ti-BPPs were employed. The cell active area was 4 cm^2 and in both setups and tests were carried out at 80ºC and ambient pressure. The polarization curves were measured galvanostatically according to the JRC EU-harmonized procedure,[49] employing a dwell and consecutive recording period of 10 s for each current step. The high-frequency resistance (HFR) was obtained from the high-frequency intercept of the Nyquist plot with the real axis and Tafel slopes are set on from a fit of the linear region between 10–100 mA cm^{-2}.

Data Availability

The data that support the findings of this study are available within the article and its Supplementary Information files. All other relevant data supporting the findings of this study are available from the corresponding authors upon request.

References

1. IRENA. *Decarbonising end-use sectors: Practical insights on green hydrogen. Contributions to Management Science* (2021).
2. Stamenkovic, V. R., Strmcnik, D., Lopes, P. P. & Markovic, N. M. Energy and fuels from electrochemical interfaces. *Nat. Mater.* **16**, 57–69 (2017).
3. Carmo, M., Fritz, D. L., Mergel, J. & Stolten, D. A comprehensive review on PEM water electrolysis. *Int. J. Hydrogen Energy* **38**, 4901–4934 (2013).
4. Reier, T. *et al.* Electrocatalytic Oxygen Evolution Reaction in Acidic Environments – Reaction Mechanisms and Catalysts. *Adv. Energy Mater.* **7**, 1601275 (2017).
5. Katsounaros, I., Cherevko, S., Zeradjanin, A. R. & Mayrhofer, K. J. J. J. Oxygen Electrochemistry as a Cornerstone for Sustainable Energy Conversion. *Angew. Chemie - Int. Ed.* **53**, 102–121 (2014).
6. Retuerto, M. *et al.* Na-doped ruthenium perovskite electrocatalysts with improved oxygen evolution activity and durability in acidic media. *Nat. Commun.* **10**, 2041 (2019).
7. Lettenmeier, P. *et al.* Nanosized IrOx-Ir Catalyst with Relevant Activity for Anodes of Proton Exchange Membrane Electrolysis Produced by a Cost-Effective Procedure. *Angew. Chemie - Int. Ed.* **55**, 742–746 (2016).
8. Abbott, D. F. *et al.* Iridium Oxide for the Oxygen Evolution Reaction: Correlation between Particle Size, Morphology, and the Surface Hydroxo Layer from Operando XAS. *Chem. Mater.* **28**, 6591–6604 (2016).
9. Matthey, J. *PGM market report May 2021*. (2021).
10. Seitz, L. C. *et al.* A highly active and stable IrOx/SrIrO3 catalyst for the oxygen evolution reaction. *Science (80-.).* **353**, 1011–1014 (2016).
11. Geiger, S. *et al.* The stability number as a metric for electrocatalyst stability benchmarking. *Nat. Catal.* **1**, 508–515 (2018).

12. Grimaud, A. *et al.* Activation of surface oxygen sites on an iridium-based model catalyst for the oxygen evolution reaction. *Nat. Energy* **2**, 16189 (2016).
13. Yang, L. *et al.* Efficient oxygen evolution electrocatalysis in acid by a perovskite with face-sharing IrO6 octahedral dimers. *Nat. Commun.* **9**, 5236 (2018).
14. Liang, X. *et al.* Activating Inert, Nonprecious Perovskites with Iridium Dopants for Efficient Oxygen Evolution Reaction under Acidic Conditions. *Angew. Chemie - Int. Ed.* **58**, 7631–7635 (2019).
15. Song, H. J., Yoon, H., Ju, B. & Kim, D. W. D.-W. Highly Efficient Perovskite-Based Electrocatalysts for Water Oxidation in Acidic Environments: A Mini Review. *Adv. Energy Mater.* **11**, 1–13 (2021).
16. Zhang, R. *et al.* First Example of Protonation of Ruddlesden–Popper Sr2IrO4: A Route to Enhanced Water Oxidation Catalysts. *Chem. Mater.* **32**, 3499–3509 (2020).
17. Ma, C.-L. *et al.* Surface Reconstruction for Forming the [IrO6]–[IrO6] Framework: Key Structure for Stable and Activated OER Performance in Acidic Media. *ACS Appl. Mater. Interfaces* **13**, 29654–29663 (2021).
18. Li, N. *et al.* Identification of the Active-Layer Structures for Acidic Oxygen Evolution from 9R-BaIrO3 Electrocatalyst with Enhanced Iridium Mass Activity. *J. Am. Chem. Soc.* **143**, 18001–18009 (2021).
19. Chen, Y. *et al.* Exceptionally active iridium evolved from a pseudo-cubic perovskite for oxygen evolution in acid. *Nat. Commun.* **10**, 572 (2019).
20. Edgington, J., Schweitzer, N., Alayoglu, S. & Seitz, L. C. Constant Change: Exploring Dynamic Oxygen Evolution Reaction Catalysis and Material Transformations in Strontium Zinc Iridate Perovskite in Acid. *J. Am. Chem. Soc.* **143**, 9961–9971 (2021).
21. Kayser, P. *et al.* Crystal Structure, Phase Transitions, and Magnetic Properties of Iridium Perovskites Sr2MIrO6 (M = Ni, Zn). *Inorg. Chem.* **52**, 11013–11022 (2013).
22. Kayser, P. *et al.* Crystal and Magnetic Structure of Sr2MIrO6 (M = Ca, Mg) Double Perovskites – A Neutron Diffraction Study. *Eur. J. Inorg. Chem.* **2014**, 178–185 (2014).
23. Diaz-Morales, O. *et al.* Iridium-based double perovskites for efficient water oxidation in acid media. *Nat. Commun.* **7**, 12363 (2016).
24. McCrory, C. C. L. L., Jung, S., Peters, J. C. & Jaramillo, T. F. Benchmarking

heterogeneous electrocatalysts for the oxygen evolution reaction. *J. Am. Chem. Soc.* **135**, 16977–16987 (2013).

25. Liang, X. *et al.* Perovskite-Type Solid Solution Nano-Electrocatalysts Enable Simultaneously Enhanced Activity and Stability for Oxygen Evolution. *Adv. Mater.* **32**, 1–8 (2020).
26. Retuerto, M. *et al.* How oxidation state and lattice distortion influence the oxygen evolution activity in acid of iridium double perovskites. *J. Mater. Chem. A* **6**, 2980–2990 (2021).
27. Elmaalouf, M. *et al.* The origin of the high electrochemical activity of pseudo-amorphous iridium oxides. *Nat. Commun.* **12**, 3935 (2021).
28. Lebedev, D. *et al.* Highly Active and Stable Iridium Pyrochlores for Oxygen Evolution Reaction. *Chem. Mater.* **29**, 5182–5191 (2017).
29. Weber, D. *et al.* Trivalent iridium oxides: Layered triangular lattice iridate K0.75Na0.25IrO2 and Oxyhydroxide IrOOH. *Chem. Mater.* **29**, 8338–8345 (2017).
30. Weber, D. *et al.* IrOOH nanosheets as acid stable electrocatalysts for the oxygen evolution reaction. *J. Mater. Chem. A* **6**, 21558–21566 (2018).
31. Zhang, R. *et al.* A Dissolution/Precipitation Equilibrium on the Surface of Iridium-Based Perovskites Controls Their Activity as Oxygen Evolution Reaction Catalysts in Acidic Media. *Angew. Chemie - Int. Ed.* **131**, 4619–4623 (2019).
32. Willinger, E., Massué, C., Schlögl, R. & Willinger, M. G. Identifying Key Structural Features of IrO x Water Splitting Catalysts. *J. Am. Chem. Soc.* **139**, 12093–12101 (2017).
33. Zhang, R. *et al.* Importance of Water Structure and Catalyst-Electrolyte Interface on the Design of Water Splitting Catalysts. *Chem. Mater.* **31**, 8248–8259 (2019).
34. Pavlovic, Z., Ranjan, C., Gao, Q., van Gastel, M. & Schlögl, R. Probing the Structure of a Water-Oxidizing Anodic Iridium Oxide Catalyst using Raman Spectroscopy. *ACS Catal.* **6**, 8098–8105 (2016).
35. Song, C. W., Lim, J., Bae, H. Bin & Chung, S.-Y. Discovery of crystal structure–stability correlation in iridates for oxygen evolution electrocatalysis in acid. *Energy Environ. Sci.* **13**, 4178–4188 (2020).
36. Zaman, W. Q. *et al.* Iridium substitution in nickel cobaltite renders high mass specific OER activity and durability in acidic media. *Appl. Catal. B Environ.* **244**,

295–302 (2019).
37. Fan, Z. *et al.* Extraordinary acidic oxygen evolution on new phase 3R-iridium oxide. *Joule* **5**, 3221–3234 (2021).
38. Gao, J. *et al.* Breaking Long-Range Order in Iridium Oxide by Alkali Ion for Efficient Water Oxidation. *J. Am. Chem. Soc.* **141**, 3014–3023 (2019).
39. Schuler, T. *et al.* Hierarchically Structured Porous Transport Layers for Polymer Electrolyte Water Electrolysis. *Adv. Energy Mater.* **10**, 1903216 (2020).
40. Scheepers, F. *et al.* Improving the Efficiency of PEM Electrolyzers through Membrane-Specific Pressure Optimization. *Energies* **13**, 612 (2020).
41. Siracusano, S. *et al.* Chemically stabilised extruded and recast short side chain Aquivion® proton exchange membranes for high current density operation in water electrolysis. *J. Memb. Sci.* **578**, 136–148 (2019).
42. Bernt, M., Schröter, J., Möckl, M. & Gasteiger, H. A. Analysis of Gas Permeation Phenomena in a PEM Water Electrolyzer Operated at High Pressure and High Current Density. *J. Electrochem. Soc.* **167**, 124502 (2020).
43. Lettenmeier, P. *et al.* Durable Membrane Electrode Assemblies for Proton Exchange Membrane Electrolyzer Systems Operating at High Current Densities. *Electrochim. Acta* **210**, 502–511 (2016).
44. Stiber, S. *et al.* A high-performance, durable and low-cost proton exchange membrane electrolyser with stainless steel components. *Energy Environ. Sci.* **15**, 109–122 (2022).
45. Oh, H. S. H.-S., Nong, H. N., Reier, T., Gliech, M. & Strasser, P. Oxide-supported Ir nanodendrites with high activity and durability for the oxygen evolution reaction in acid PEM water electrolyzers. *Chem. Sci.* **6**, 3321–3328 (2015).
46. Hegge, F. *et al.* Efficient and Stable Low Iridium Loaded Anodes for PEM Water Electrolysis Made Possible by Nanofiber Interlayers. *ACS Appl. Energy Mater.* **3**, 8276–8284 (2020).
47. Bernt, M., Siebel, A. & Gasteiger, H. A. Analysis of Voltage Losses in PEM Water Electrolyzers with Low Platinum Group Metal Loadings. *J. Electrochem. Soc.* **165**, F305 (2018).
48. Möckl, M. *et al.* Durability Testing of Low-Iridium PEM Water Electrolysis Membrane Electrode Assemblies. *J. Electrochem. Soc.* **169**, 064505 (2022).
49. Malkow, T., Pilenga, A. & Tsotridis, G. EU Harmonised Polarisation Curve Test

Method for Low Temperature Water Electrolysis. *Publications Office of the European Union* (2018) doi:10.2760/179509.

50. Rietveld, H. M. A profile refinement method for nuclear and magnetic structures. *J. Appl. Crystallogr.* **2**, 65–71 (1969).

51. Dinnebier, R. & Rodríguez-carvajal, J. *Commission on Powder Diffraction. Rietveld Refinement from Powder Diffraction Data CPD Chairman ' s Message 26 CPD projects From the Editor of Newsletter 26*. *Powder Diffraction* (2001).

52. Claudel, F. *et al.* Degradation Mechanisms of Oxygen Evolution Reaction Electrocatalysts: A Combined Identical-Location Transmission Electron Microscopy and X-ray Photoelectron Spectroscopy Study. *ACS Catal.* **9**, 4688–4698 (2019).

53. Wagner, C. D. *et al.* Empirical atomic sensitivity factors for quantitative analysis by electron spectroscopy for chemical analysis. *Surf. Interface Anal.* **3**, 211–225 (1981).

54. Dent, A. J. *et al.* Performance of B18, the Core EXAFS Bending Magnet beamline at Diamond. *J. Phys. Conf. Ser.* **430**, 012023 (2013).

55. Sardar, K. *et al.* Water-Splitting Electrocatalysis in Acid Conditions Using Ruthenate-Iridate Pyrochlores. *Angew. Chemie - Int. Ed.* **126**, 11140–11144 (2014).

56. Ravel, B. & Newville, M. ATHENA , ARTEMIS , HEPHAESTUS : data analysis for X-ray absorption spectroscopy using IFEFFIT. *J. Synchrotron Radiat.* **12**, 537–541 (2005).

57. Ankudinov, A. L., Ravel, B., Rehr, J. J. & Conradson, S. D. Real-space multiple-scattering calculation and interpretation of x-ray-absorption near-edge structure. *Phys. Rev. B* **58**, 7565–7576 (1998).

58. Stiber, S. *et al.* Porous Transport Layers for Proton Exchange Membrane Electrolysis Under Extreme Conditions of Current Density, Temperature, and Pressure. *Adv. Energy Mater.* **11**, 2100630 (2021).

59. Lettenmeier, P. *et al.* Coated Stainless Steel Bipolar Plates for Proton Exchange Membrane Electrolyzers. *J. Electrochem. Soc.* **163**, F3119–F3124 (2016).

Acknowledgements

We acknowledge PROMET-H2 project. This project has received funding from the European Union's Horizon 2020 research and innovation programme under grant agreement No 862253. The Deputyship for Research & Innovation, Ministry of Education of Saudi Arabia is acknowledged for funding this research work through the project number 341. Financial support from grants PID2020-116712RB-C21and PID2019-103967RJ-I00 funded by MCIN/AEI/10.13039/501100011033 is acknowledged. M.R. thanks RyC2019-026521 from MCIN/AEI/10.13039/501100011033 and "ESF Investing in your future" and L´Oréal-UNESCO for a "For Women in Science" Fellowship. The authors acknowledge Diamond Light Source for time on Beamline B18 under the proposal SP27733-1. The authors wish to acknowledge the Deutsche Akademische Austausch Dienst (DAAD), Scholarship code number 57540124.

Authors Contributions Statement

MR and LP contributed equally to the work. MR, LP and SR conceived the idea of the project. ATM, PK, JAA prepared the samples. MR, MAS and MM conducted the RDE experiments. LP made the TEM study. JT, VW, SS, DGS, ASG and KAF made the PEMWE measurements. MAP made the XPS study. PF, DG and VC made the *in situ* XAS study. MR, LP and SR co-wrote the paper. MR and SR supervised the project.

Competing interests Statement

The authors declare no competing interests.

Figure Legends/Captions

Figure 1| OER performance. (a) Current densities obtained for Sr_2MIrO_6 (M= Ca, Mg and Zn). Inset: Generation of oxygen in Sr_2CaIrO_6 in the RDE configuration at different potentials. (b) Tafel plots of the Sr_2MIrO_6 catalysts and SoA catalysts from references.[12–14,19,23,28] (c) Ir mass-specific OER activity for Sr_2MIrO_6 compared to catalysts of reference[7]. (d) Tafel slope (upper panel), potential at 10 $mAcm^{-2}$ (middle panel) and Ir mass-specific activity at 1.525 V (bottom panel) of the state-of-the-art OER Ir-mixed oxide catalysts reported in the literature (appropriate references are given in Table S1).

Figure 2| Evolution of Sr_2CaIrO_6 in the electrolyte and during the OER. (a) Fresh Sr_2CaIrO_6, (b) immersed in the electrolyte (Sr_2CaIrO_6-Elec), (c) after 100 OER cycles (Sr_2CaIrO_6-100) and (d) after 5000 OER cycles (Sr_2CaIrO_6-5000). Upper panel: Schematic view of the surface reconstruction. Central Panels: IL-TEM micrographs of the same region, SAED and EDX. Bottom Panel: XPS spectra showing the evolution of the Ir 4*f* region and the relative surface atomic composition of Sr, Ca, and Ir.

Figure 3| Morphology and structure of the hollow Ir-O particles. IL-TEM of a region of Sr_2CaIrO_6 (a) before and (b) after 100 OER cycles. (c) HRTEM of the initial catalyst. (d), (e), (f) TEM, STEM and EDX images of the hollow regions composed of Ir and O. Inset Figure d: SAED pattern. Note that diffraction rings at 2.1 and 1.1 Å appear after long-term exposure due to Ir^0 species formed by the reduction of Ir^{n+} phases under the electron beam.[32] (g) Aberration-corrected STEM-HAADF image and (h) the corresponding filtered image with a magnification of a short-range ordered region between Ir cations of the catalyst after 100 cycles.

Figure 4| *In situ* monitoring of the catalyst evolution during the OER. (a) XANES signals of the Ir L_3-edge of Sr_2CaIrO_6-Elec, Sr_2CaIrO_6-2000, and IrO_2 standard. (b) Evolution of the white line position, related to the evolution of the oxidation state (black) and the intensity (red) of the XANES signal around 11220 eV during cycling. Inset: Zoom on white line position and intensity changes of the XANES signal observed in the whole series of Sr_2CaIrO_6 spectra collected during cycling. (c) Evolution of the FT-EXAFS region during OER cycling. (d) FT-EXAFS of Sr_2CaIrO_6-Elec, Sr_2CaIrO_6-2000 together with the simulated data of Sr_2CaIrO_6, IrO_2 and IrOOH.

Figure 5| Assessment of OER performance during PEMWE. PEMWE measurements with the Sr_2CaIrO_6 anode (0.4 mg_{Ir} cm^{-2}) and Pt/C (commercial) cathode (0.4 mg_{Pt} cm^{-2}): (a) Cell potential (E_{cell}) with respect to the current density (*j*) recorded galvanostatically up to 6 A cm^{-2} (overload) according to the JRC EU-harmonized procedure;[49] a dwell and consecutive recording period of 10 s was used for each current step. Reference performance values reached by Stiber et al.[44] Oh et al.[45], Bernt et al.[42] and Hegge et al.[46], using Nafion N212 based PEMWE CCMs are included. Note that [42,44,45] use higher Ir loadings. (b) E_{cell} and cell temperature (T_{cell}) evolution over time (t) (450 h) at a constant 2 A cm^{-2} (nominal load). The measurements were carried out at 80 °C and ambient pressure.

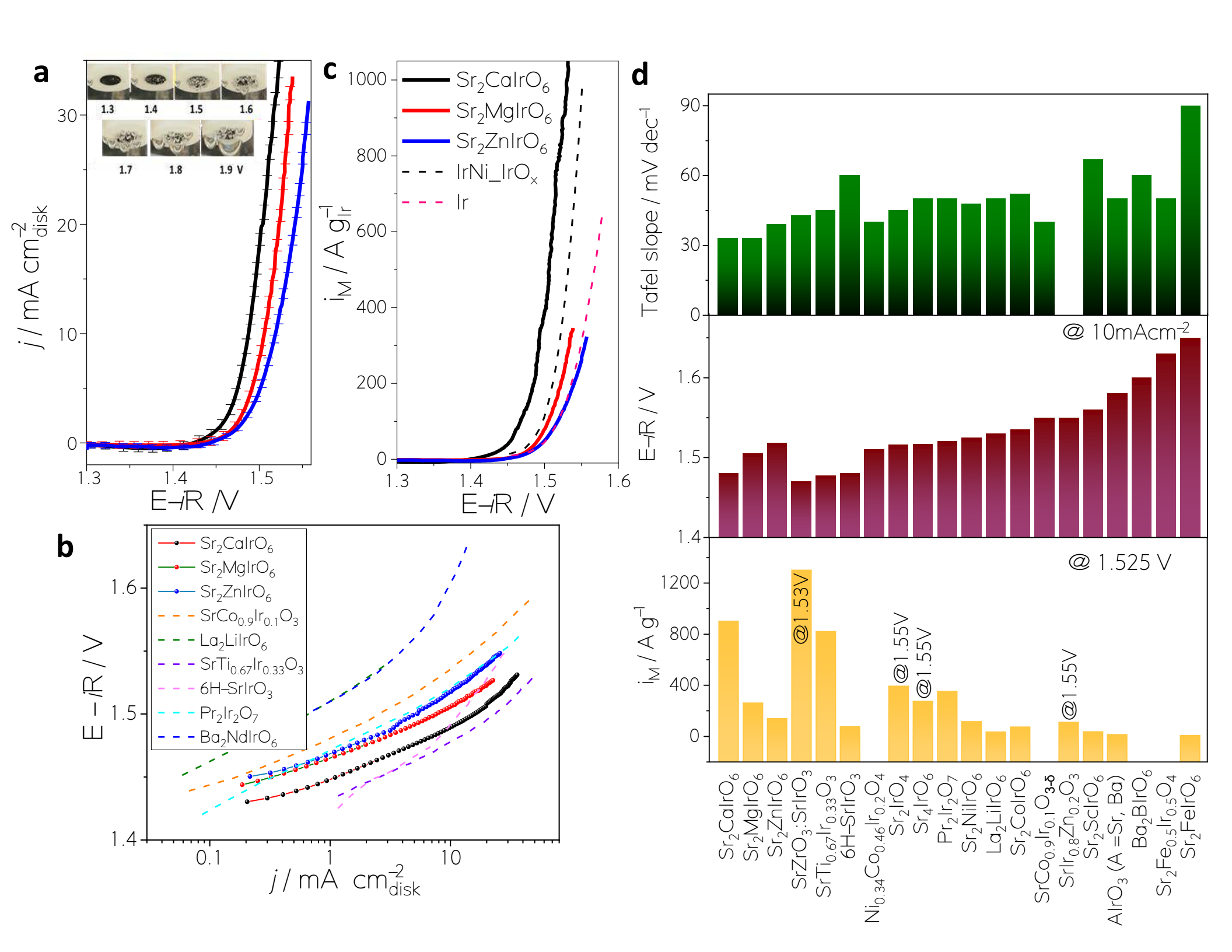
a
1.3
1.4
1.5
1.6
1.7
1.8
1.9 V
j / mA cm$^{-2}_{disk}$
E−iR /V
c
Sr$_2$CaIrO$_6$
Sr$_2$MgIrO$_6$
Sr$_2$ZnIrO$_6$
IrNi_IrO$_x$
Ir
i$_M$ / A g$^{-1}_{Ir}$
E−iR / V
b
Sr$_2$CaIrO$_6$
Sr$_2$MgIrO$_6$
Sr$_2$ZnIrO$_6$
SrCo$_{0.9}$Ir$_{0.1}$O$_3$
La$_2$LiIrO$_6$
SrTi$_{0.67}$Ir$_{0.33}$O$_3$
6H–SrIrO$_3$
Pr$_2$Ir$_2$O$_7$
Ba$_2$NdIrO$_6$
E − iR / V
j / mA cm$^{-2}_{disk}$
d
Tafel slope / mV dec^{-1}
@ 10mAcm^{-2}
E−iR / V
@ 1.525 V
i$_M$ / A g^{-1}
@1.53V
@1.55V
@1.55V
@1.55V
Sr$_2$CaIrO$_6$
Sr$_2$MgIrO$_6$
Sr$_2$ZnIrO$_6$
SrZrO$_3$:SrIrO$_3$
SrTi$_{0.67}$Ir$_{0.33}$O$_3$
6H–SrIrO$_3$
Ni$_{0.34}$Co$_{0.46}$Ir$_{0.2}$O$_4$
Sr$_2$IrO$_4$
Sr$_4$IrO$_6$
Pr$_2$Ir$_2$O$_7$
Sr$_2$NiIrO$_6$
La$_2$LiIrO$_6$
Sr$_2$CoIrO$_6$
SrCo$_{0.9}$Ir$_{0.1}$O$_{3-\delta}$
SrIr$_{0.8}$Zn$_{0.2}$O$_3$
Sr$_2$ScIrO$_6$
AIrO$_3$ (A =Sr, Ba)
Ba$_2$BIrO$_6$
Sr$_2$Fe$_{0.5}$Ir$_{0.5}$O$_4$
Sr$_2$FeIrO$_6$

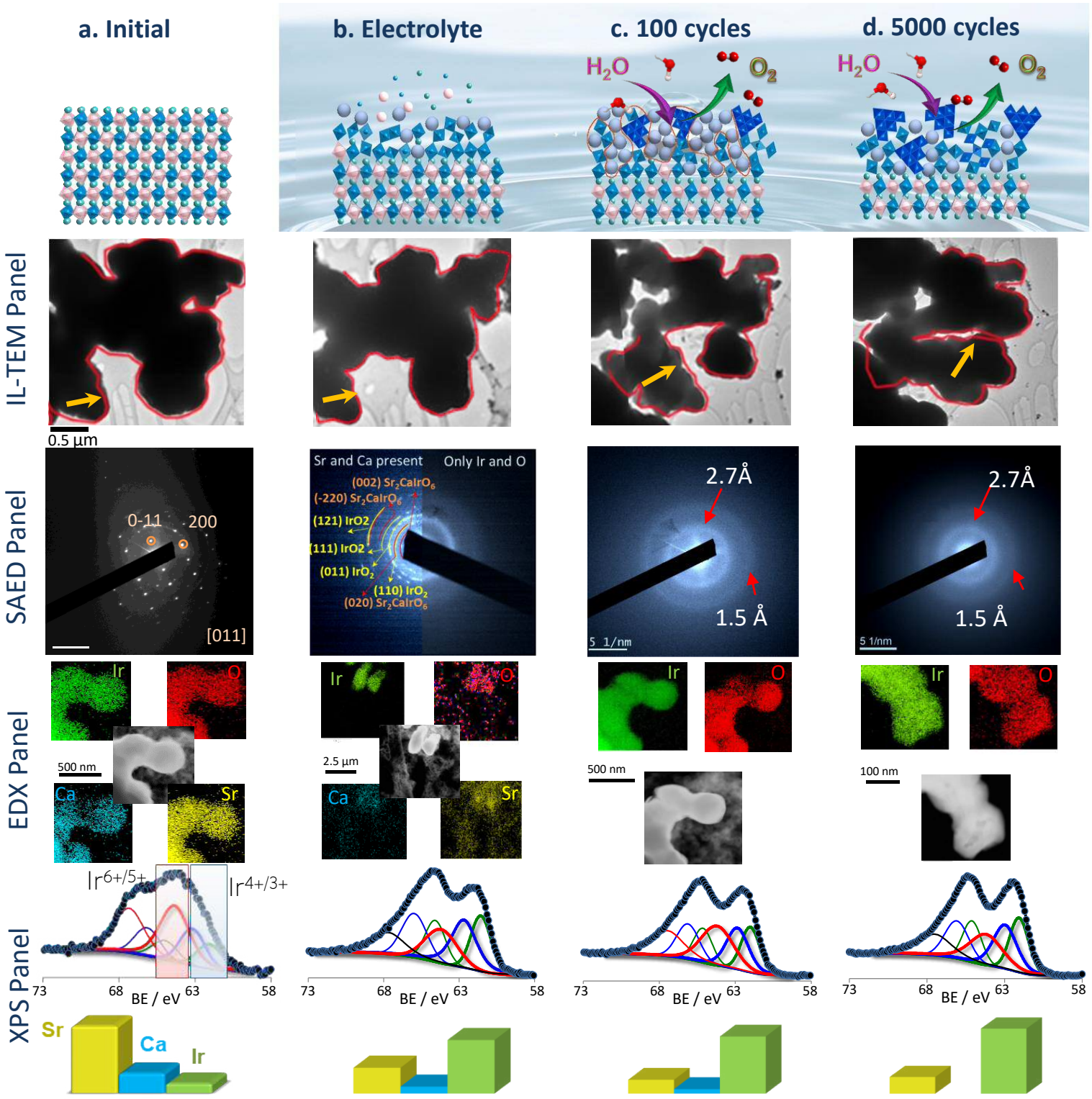
a. Initial
b. Electrolyte
c. 100 cycles
d. 5000 cycles
H2O
O2
IL-TEM Panel
0.5 μm
SAED Panel
0-11
200
[011]
Sr and Ca present
Only Ir and O
(002) Sr2CaIrO6
(-220) Sr2CaIrO6
(121) IrO2
(111) IrO2
(011) IrO2
(110) IrO2
(020) Sr2CaIrO6
2.7Å
1.5 Å
5 1/nm
EDX Panel
Ir
O
Ca
Sr
500 nm
2.5 μm
100 nm
XPS Panel
Ir6+/5+
Ir4+/3+
73
68
63
58
BE / eV
Sr
Ca
Ir

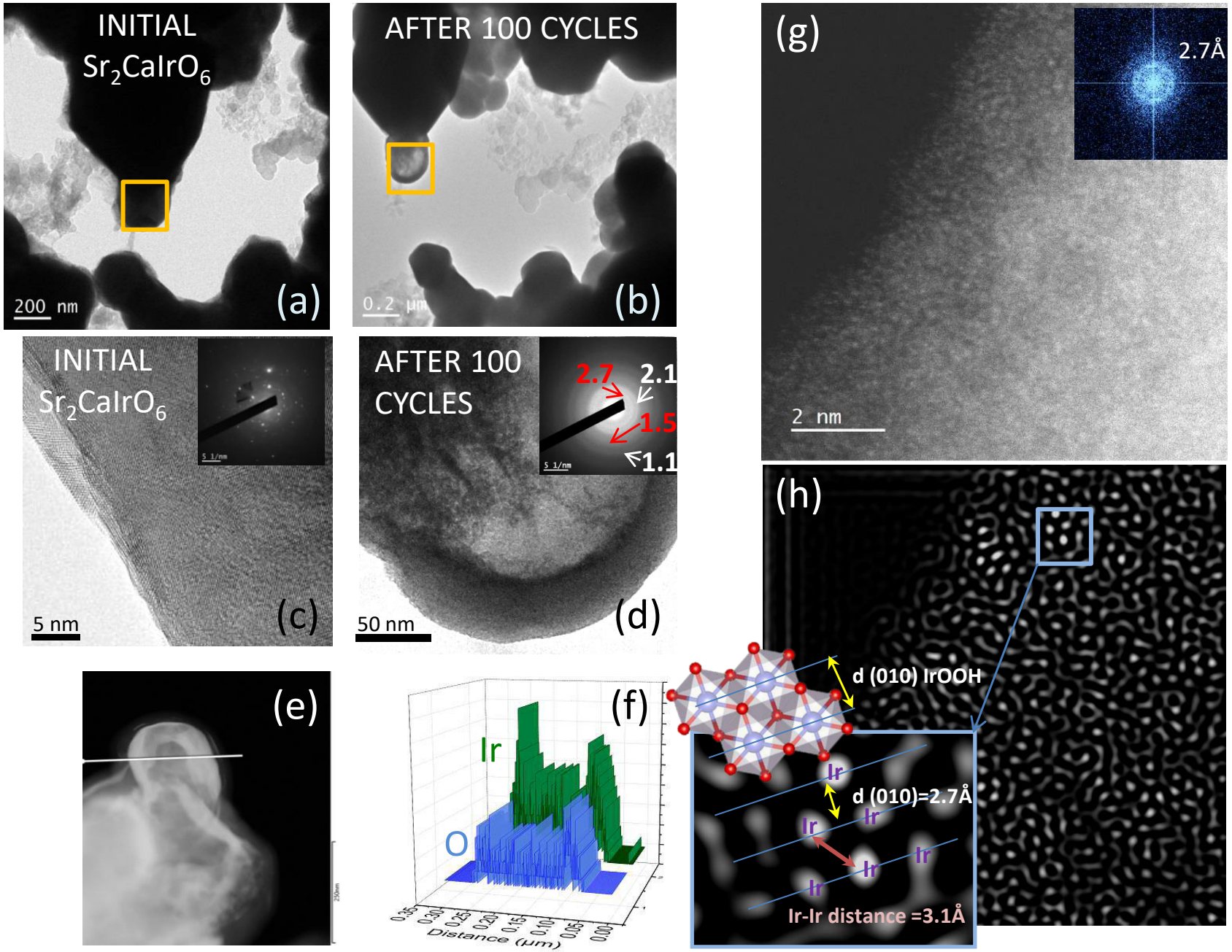
INITIAL
Sr_2CaIrO_6
200 nm
(a)
AFTER 100 CYCLES
0.2 µm
(b)
(g)
2.7Å
2 nm
INITIAL
Sr_2CaIrO_6
5 nm
(c)
AFTER 100
CYCLES
2.7
2.1
1.5
1.1
50 nm
(d)
(h)
d (010) IrOOH
d (010)=2.7Å
Ir-Ir distance =3.1Å
(e)
(f)
Ir
O
Distance (µm)

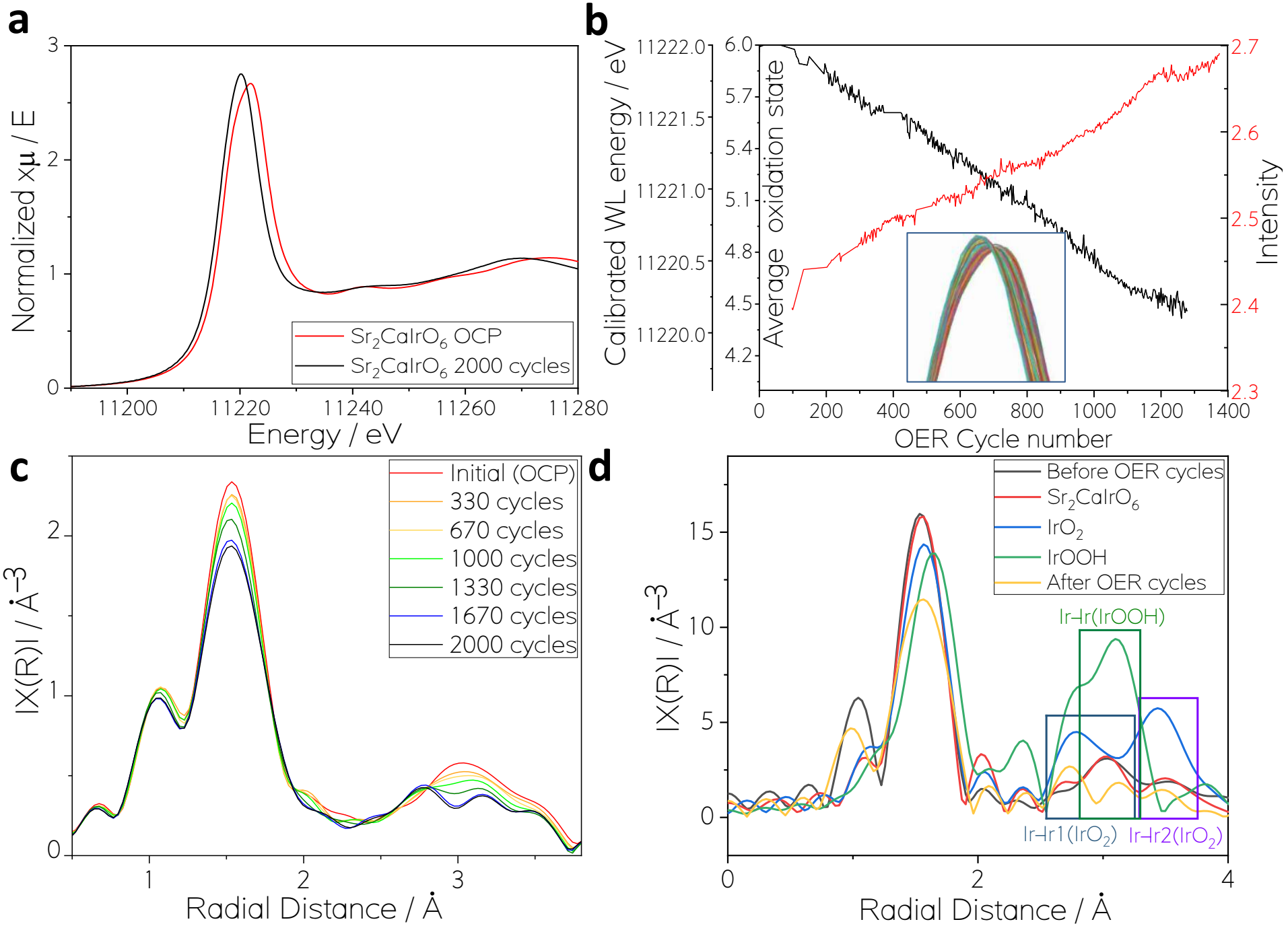
a
Normalized xμ / E
Energy / eV
Sr2CaIrO6 OCP
Sr2CaIrO6 2000 cycles
b
Calibrated WL energy / eV
Average oxidation state
Intensity
OER Cycle number
c
|X(R)| / Å−3
Radial Distance / Å
Initial (OCP)
330 cycles
670 cycles
1000 cycles
1330 cycles
1670 cycles
2000 cycles
d
|X(R)| / Å−3
Radial Distance / Å
Before OER cycles
Sr2CaIrO6
IrO2
IrOOH
After OER cycles
Ir–Ir(IrOOH)
Ir–Ir1(IrO2)
Ir–Ir2(IrO2)

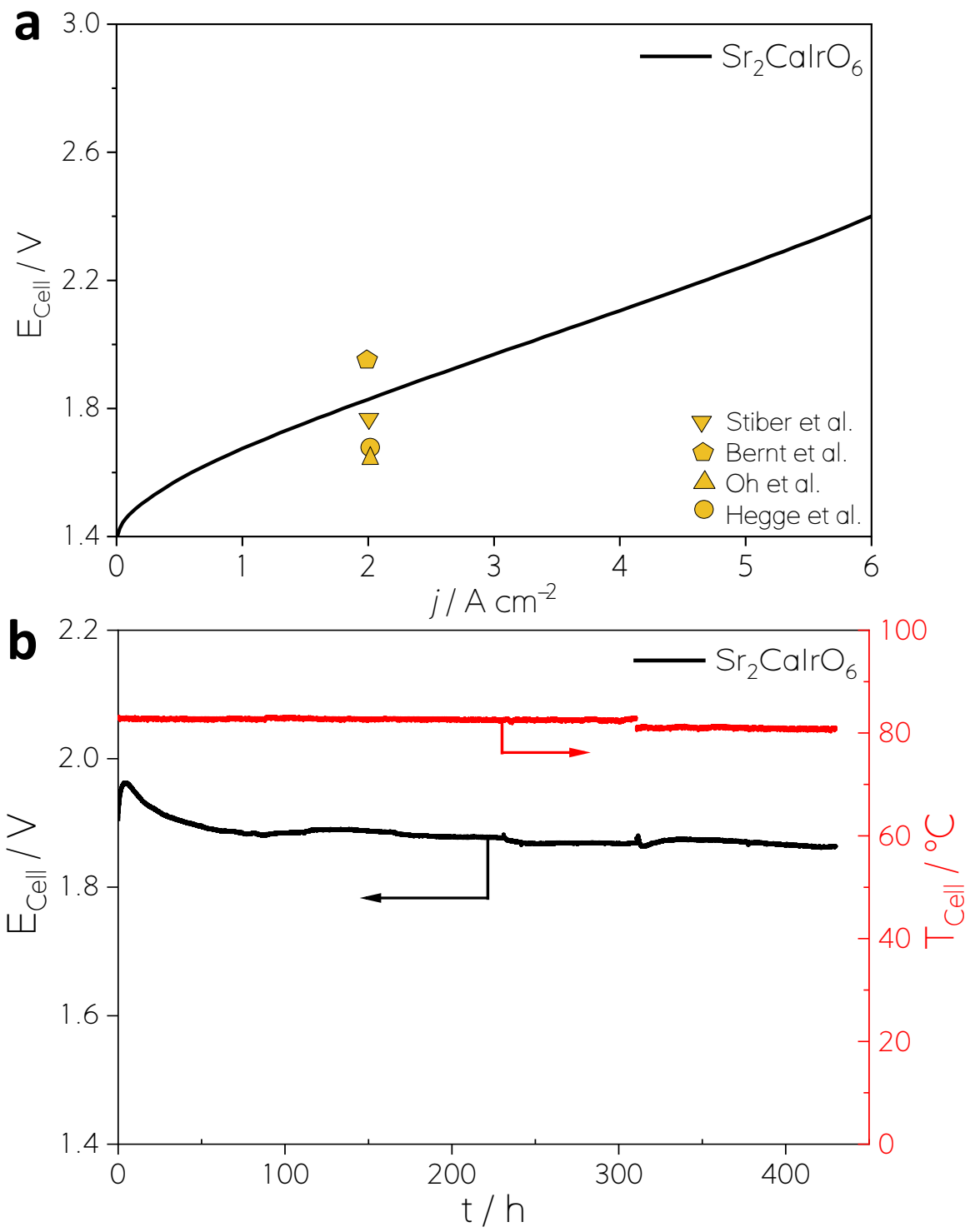
a
3.0
2.6
2.2
1.8
1.4
E_{Cell} / V
0
1
2
3
4
5
6
j / A cm^{-2}
Sr_2CaIrO_6
Stiber et al.
Bernt et al.
Oh et al.
Hegge et al.
b
2.2
2.0
1.8
1.6
1.4
E_{Cell} / V
0
100
200
300
400
t / h
100
80
60
40
20
0
T_{Cell} / °C
Sr_2CaIrO_6